nature nanotechnology

Article

https://doi.org/10.1038/s41565-023-01513-0

A wearable aptamer nanobiosensor for non-invasive female hormone monitoring

In the format provided by the authors and unedited

Table of Content

Supplementary Note 1 | Optimization and characterization of the estradiol sensing.

Optimization of the MXene layer printing. 1 mg ml^{-1} MXene ink was used for inkjet printing the MXene film with different layers (0, 2, 4, and 6 layers). Current responses measured with square wave voltammogram (SWV) show that the AuNPs-MXene electrode with 4 layers of MXene showed the largest current response towards 50 pM estradiol compared to other ones (**Supplementary Fig. 15**). The response current substantially increased with the MXene increased to 4 layers due to the high conductivity and electrochemical catalytic activities of MXene. However, the response current dropped with the MXene layer further increased to 6 layers, largely due to the stacked MXene which blocked the adsorption site of SH-ssDNA adsorb onto AuNPs surface by Au-SH bond.

Optimization estradiol sensor surface modification conditions. In order to maximize the sensitivity and efficiency of the estradiol sensor, the incubation time of MCH and MB-ssDNA, and concentrations of SH-ssDNA and MB-ssDNA were optimized. MCH was used to block the extra Au site to avoid non-selective adsorption of other interferences, and to ensure that MB-ssDNA was efficiently bonded to the aptamer on the biorecognition interface. The incubation time (10, 20, 30, 40, and 50 min) of MCH and MB-ssDNA was evaluated. As shown in **Supplementary Fig. 16a**,**b**, 30 min incubation resulted in the highest response of estradiol sensing. The concentrations of SH-ssDNA and MB-ssDNA were also optimized to realize the highest efficiency (**Supplementary Fig. 16c,d**) for the estradiol sensor responses: the current increased with SH-ssDNA concentration initially and plateaued at 5 μM SH-ssDNA while the current increased with MB-ssDNA concentration on biorecognition interface and plateaued at 1 μM MB-ssDNA. Thus 5 μM SH-ssDNA and 1 μM MB-ssDNA were selected and used throughout the experiments.

Optimization of the measurement frequency for estradiol sensors. For an electrochemical sensor employing a redox moiety, the applied frequency has substantial influences on the sensor response. Varying SWV frequency offers great potential to tune the sensitivity of the sensor and switch the polarity of the resulting sensor. As shown in **Supplementary Fig 17**, the SWV peak current increases with increasing SWV frequency towards estradiol sensing and plateaus at 90 Hz. Thus, 90 Hz was used throughout the experiments.

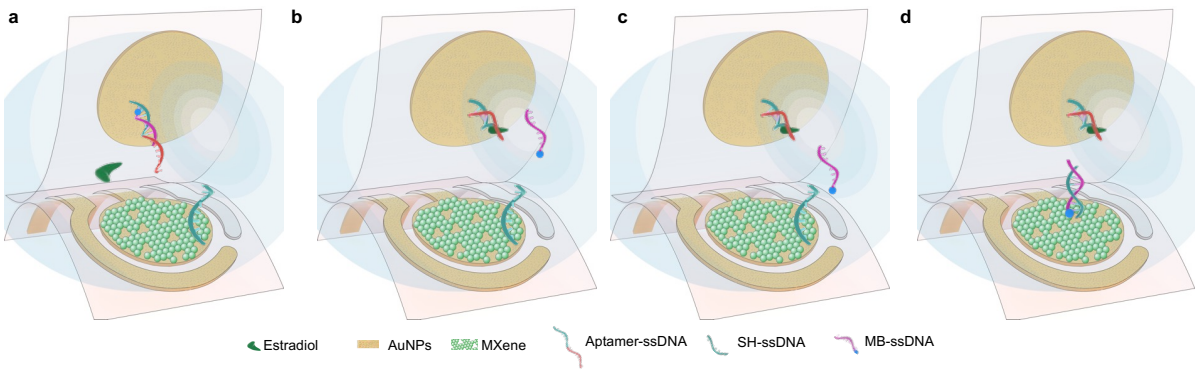

Supplementary Fig. 1 | Schematic of the working mechanism of the estradiol sensor. a, Recognition of the estradiol molecule by the aptamer on the biorecognition interface. **b**, Target recognition-induced strand displacement to release the MB-ssDNA. **c**, Recapture of the released MB-ssDNA by the SH-ssDNA on the working electrode. **d**, Electrochemical quantification of the MB from the recaptured MB-ssDNA on the working electrode.

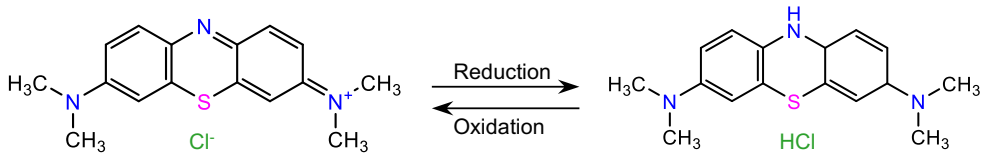

Supplementary Fig. 2 | The redox reaction of the methylene blue.

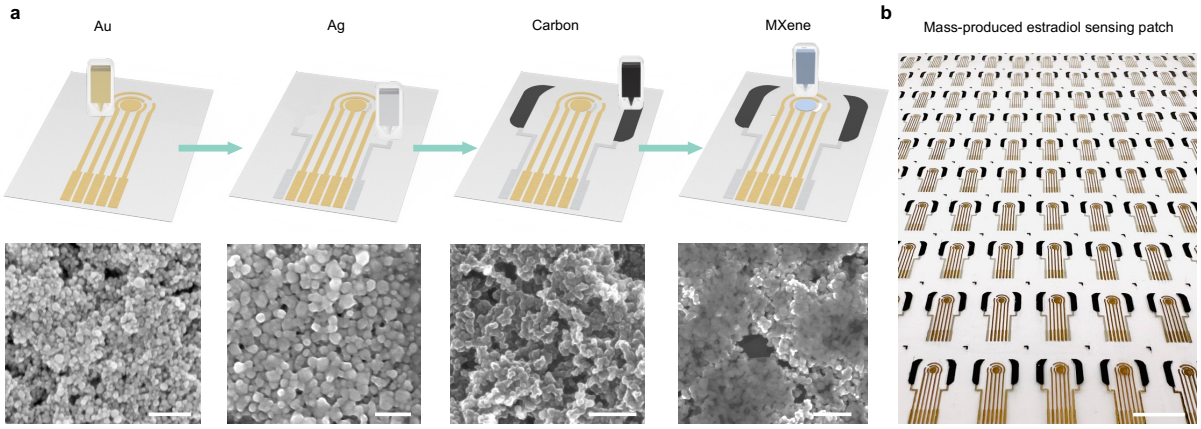

Supplementary Fig. 3 | Scalable manufacturing of the disposable sensor patch with inkjet printing. a, Schematic illustration of inkjet printing process and the corresponding scanning electron microscope (SEM) characterizations of printed nanostructure patterns. Scale bars, 200 nm. **b**, Optical image of flexible sensor patch arrays fabricated via inkjet-printing. Scale bar, 1 cm.

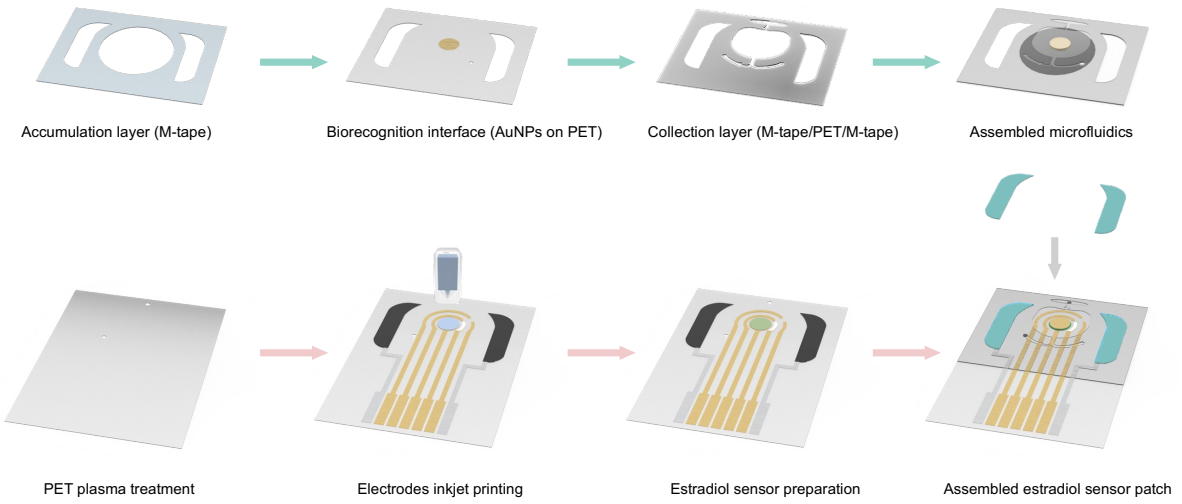

Supplementary Fig. 4 | Fabrication process of the microfluidic wearable sensor patch for autonomous female hormone analysis. PET, polyethylene terephthalate; M-tape, medical tape.

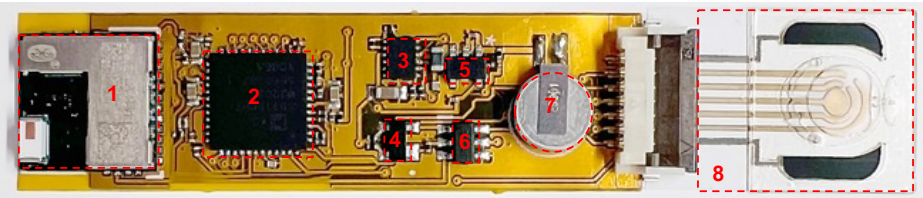

1. BLE module 2. Electrochemical analog front end 3. Boost converter 4. BJT array
5. Voltage regulator 6. Analog switch 7. Battery 8. Disposable sensor patch

Supplementary Fig. 5 | Photograph of a flatted electronic system of the wearable estradiol sensor. The read dashed boxes indicate the integrated circuit components and disposable sensor patch on the wearable system.

a

Name	Sequence (5'-3')
Aptamer-ssDNA	/5ThioMC6-D/GCTTCCAGCTTATTGAATTACACGCAGAGGGTAGCGGC TCTGCGCATTCAATTGCTGCGCGCTGAAGCGCGGAAGC
SH-ssDNA	/5ThioMC6-D/GCTTCCAGCTTATTGAATTACACGC
MB-ssDNA	GCGTGTA ATTCAATAAGCTGGAAGC/3MeBIN/

b

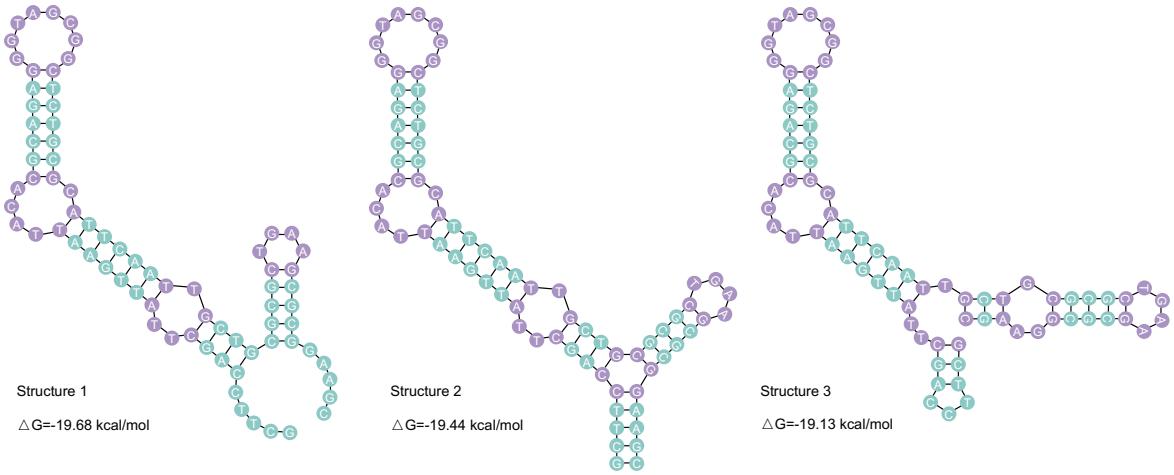

Supplementary Fig. 6 | The DNA and aptamer used in this work. a, Detailed DNA sequences. **b**, The secondary structures of the estradiol aptamer predicted using the UNAFold Web Server. ΔG, Gibbs free energy.

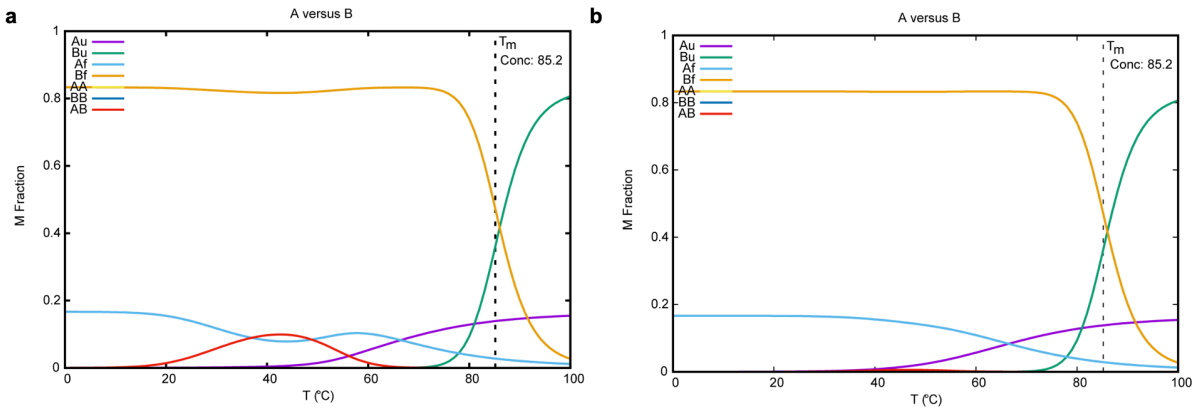

Supplementary Fig. 7. Structures analysis using "UNAFold Web Server" to predict the interaction between the MB-ssDNA and estradiol aptamer. Conditions: 1 μM MB-ssDNA (A) and 5 μM thiol-modified aptamer-ssDNA (B) in 20 mM Tris-HCl buffer (containing 50 mM NaCl and 25 mM $MgCl_2$, pH 8.0).

a, 25-base MB-ssDNA (5'-GCGTGTAATTCAATAAGCTGGAAGC-3') used as A.

b, 24-base MB-ssDNA (5'-CGTGTAATTCAATAAGCTGGAAGC-3') used as A.

M fraction, mole fraction. AB, hybridized structure of A and B; Af and Bf, folded A and B, respectively; Au and Bu, unfolded A and B, respectively.

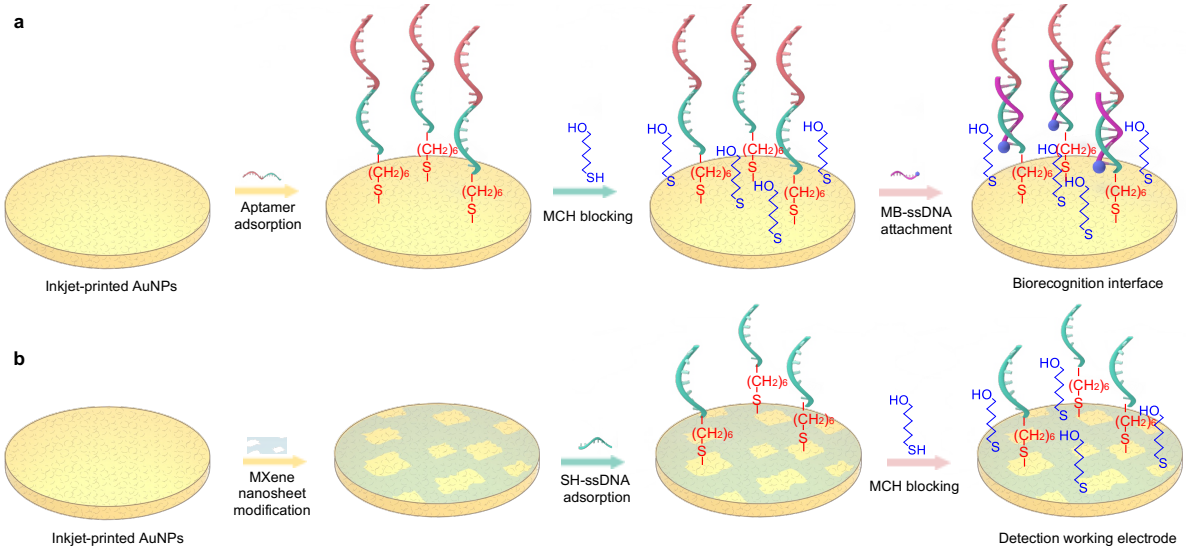

Supplementary Fig. 8 | Schematic of the surface modification procedure for automatic female hormone sensing. a, Modification procedure of biorecognition interface. **b**, Modification procedure of the detection working electrode. MCH, 6-mercapto-1-hexanol.

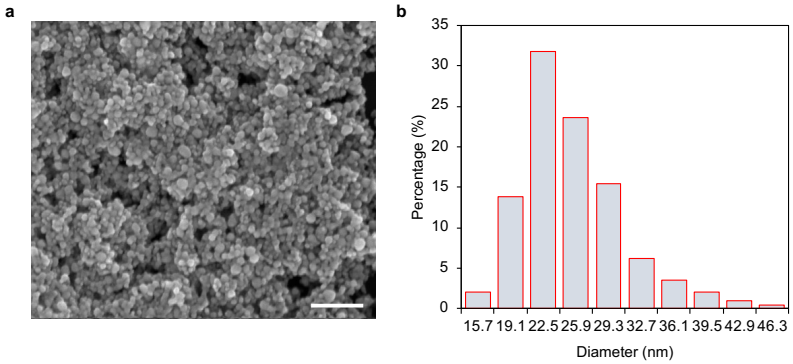

Supplementary Fig. 9 | The size distribution of the printed AuNPs. The image is representative of three independent experiments. Scale bar, 200 nm.

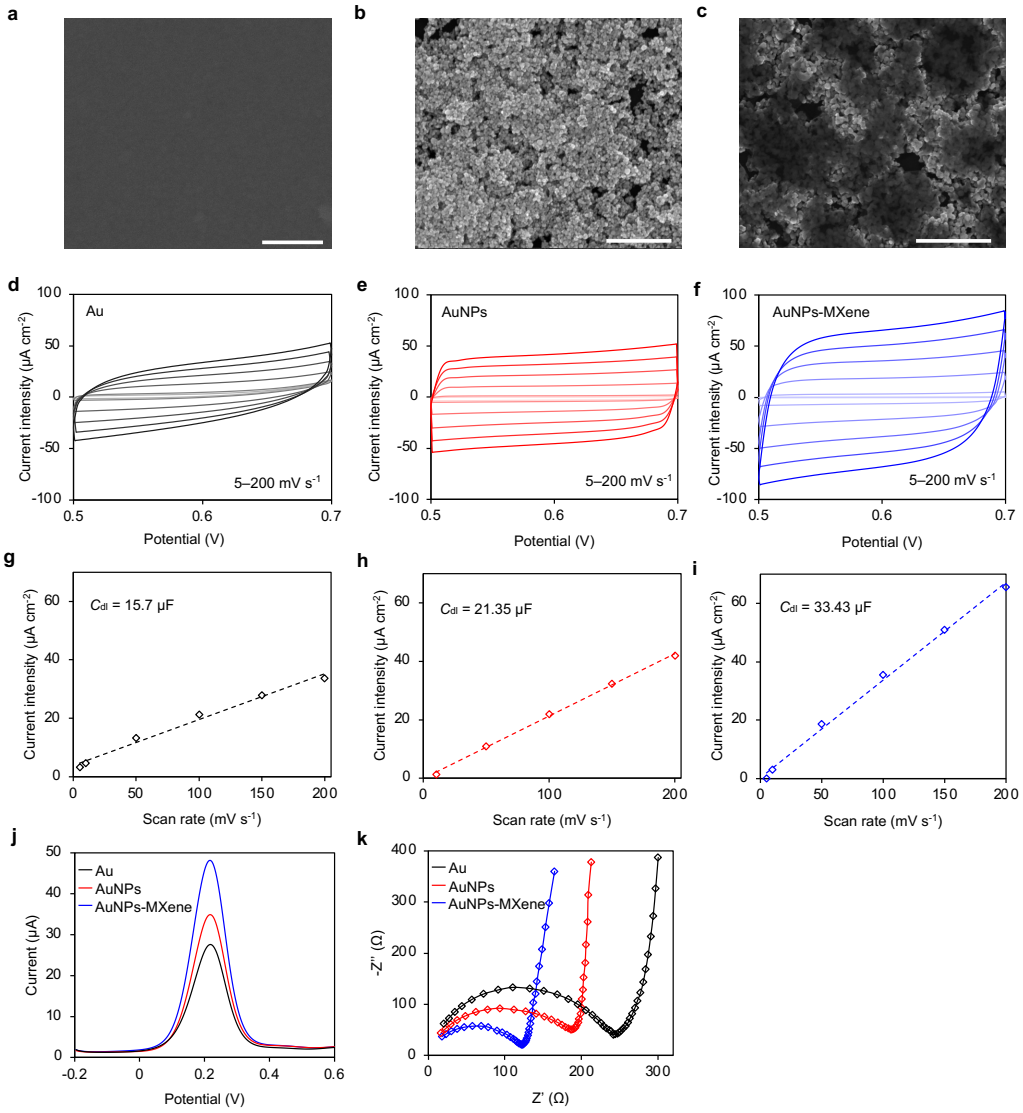

Supplementary Fig. 10 | Characterizations of the detection working electrode substrates. **a–c**, SEM images of evaporated Au (**a**), inkjet-printed AuNPs (**b**), and inkjet-printed AuNPs-MXene (**c**). The images are representative of three independent experiments. Scale bars, 500 nm. **d–i**, Cyclic voltammetry characterizations of Au (**d**), AuNPs (**e**), and AuNPs-MXene (**f**) electrodes under different scan rates (5, 10, 50, 100, 150, 200 mV s^{-1}) in artificial sweat (0.2x PBS, pH 7.4), and the corresponding calibration plots between the oxidation current density height at 0.6 V and scan rates for Au (**g**), AuNPs (**h**), and AuNPs-MXene (**i**). Dotted lines represent linear fit trendlines. C_{dl}, electrochemical double layer capacitance. **j,k**, Differential pulse voltammogram (**j**) and open circuit potential-electrochemical impedance spectroscopy (**k**) characterizations of Au, AuNPs, and AuNPs-MXene electrodes in 0.1x PBS (pH 7.4) containing 2.0 mM $K_4Fe(CN)_6/K_3Fe(CN)_6$ (1:1).

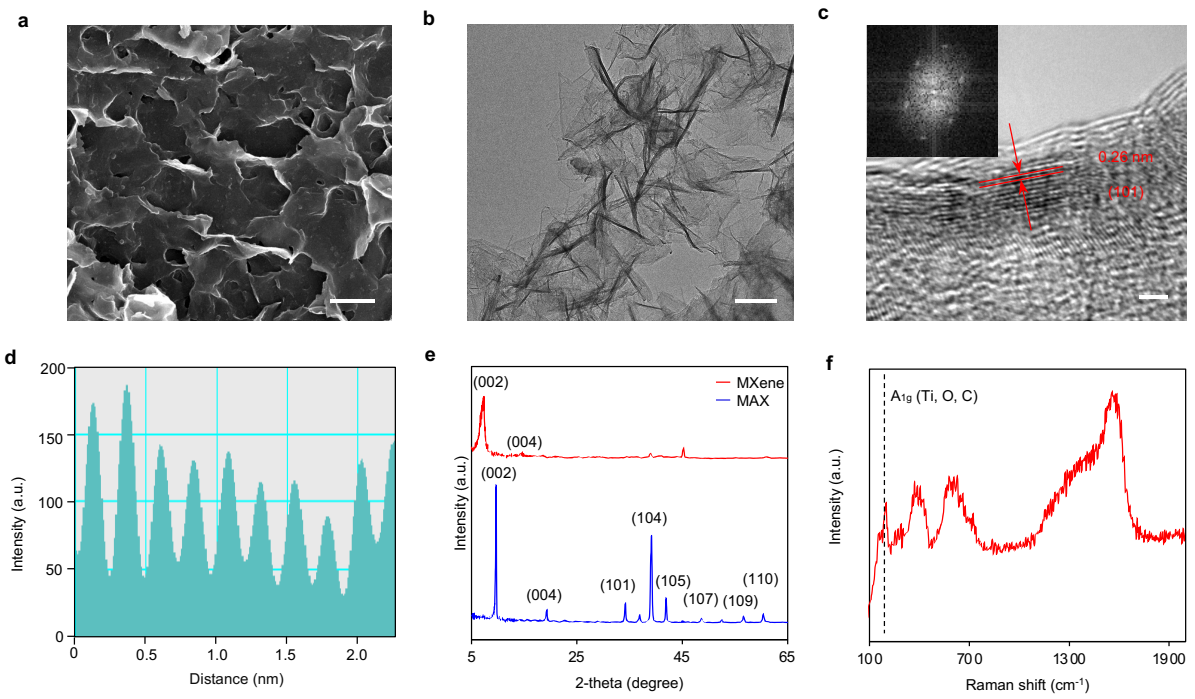

Supplementary Fig. 11 | Characterization of the MXene ink. a, SEM image of the MXene nanosheets. Scale bar, 1 μm. **b**, Transmission electron microscopy (TEM) image of the MXene nanosheets. Scale bar, 100 nm. **c,d,** High-resolution TEM image with an inset showing the selected area (electron) diffraction (SAED) pattern (**c**) and the corresponding line intensity profile (**d**). The images are representative of three independent experiments. Scale bar, 1 nm. The MXene nanosheets show a lattice fringe spacing of 0.26 nm, corresponding to the (101) crystal plane. **e**,**f**, XRD patterns (**e**) and Raman spectrum (**f**) of the MXene nanosheets.

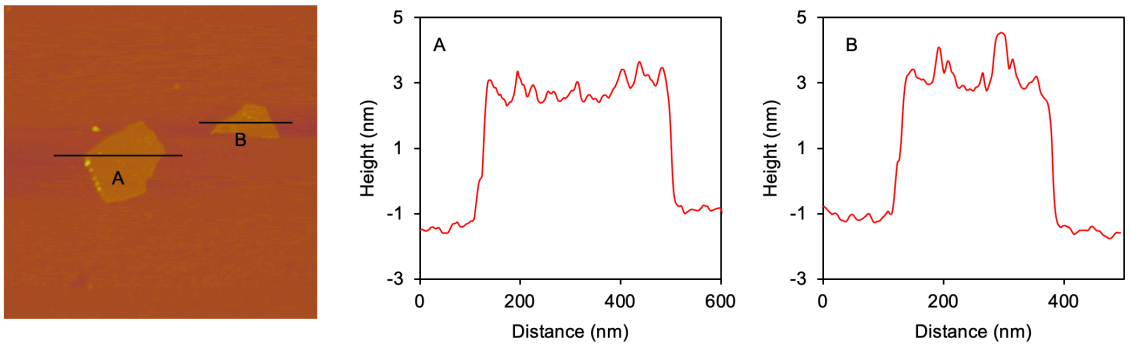

Supplementary Fig. 12 | Atomic force microscopy (AFM) image and the corresponding cross-section profiles of MXene nanosheets used in the ink.

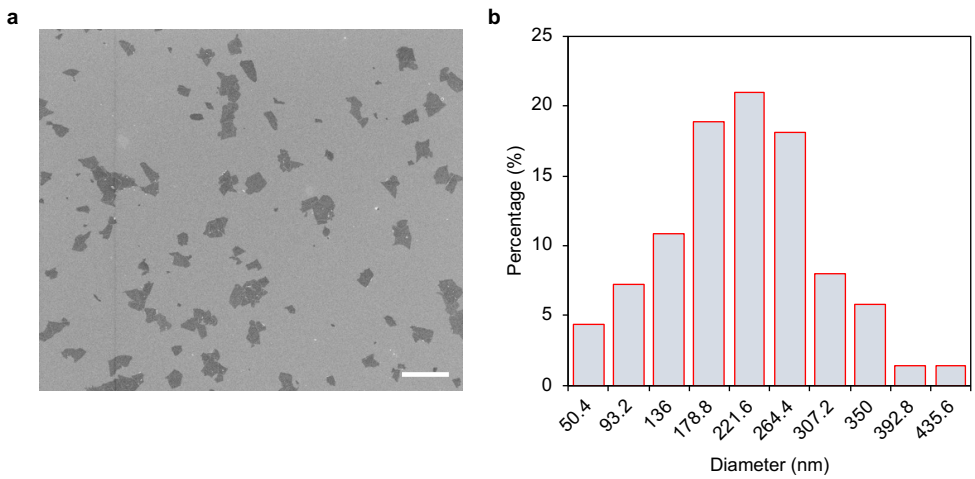

Supplementary Fig. 13 | SEM and lateral length distribution of the MXene flakes used in the ink. The images are representative of three independent experiments. Scale bar, 1 μm.

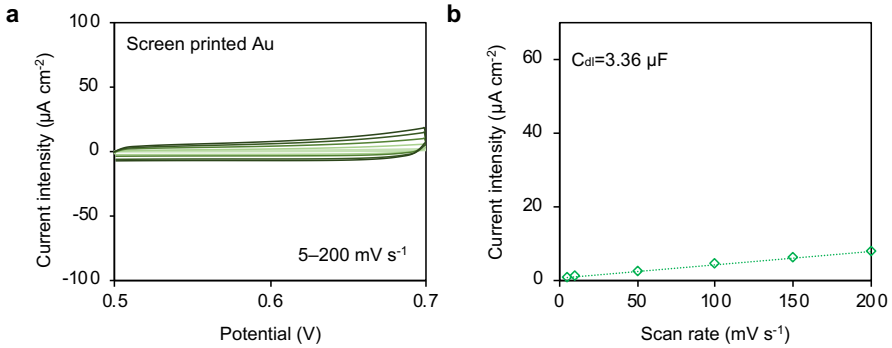

Supplementary Fig. 14 | Electrochemical characterizations of the screen-printed Au electrode. a,**b**, Cyclic voltammetry characterizations (**a**) of a screen-printed Au electrode under different scan rates (5, 10, 50, 100, 150, 200 mV s^{-1}) in artificial sweat (0.2x PBS, pH 7.4), and the corresponding calibration plots (**b**) between the oxidation current density height at 0.6 V and scan rates. Dotted lines represent linear fit trendlines.

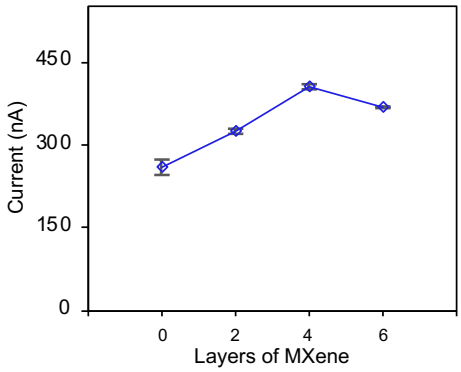

Supplementary Fig. 15 | The influence of the printed layers of MXene on the estradiol sensing. The SWV corresponding peak current height the aptamer estradiol sensors for detecting in 50 pM estradiol based on 0, 2, 4, and 6 layers of printed MXene on the AuNPs electrodes. Error bars represent the s.d. of the mean from three sensors.

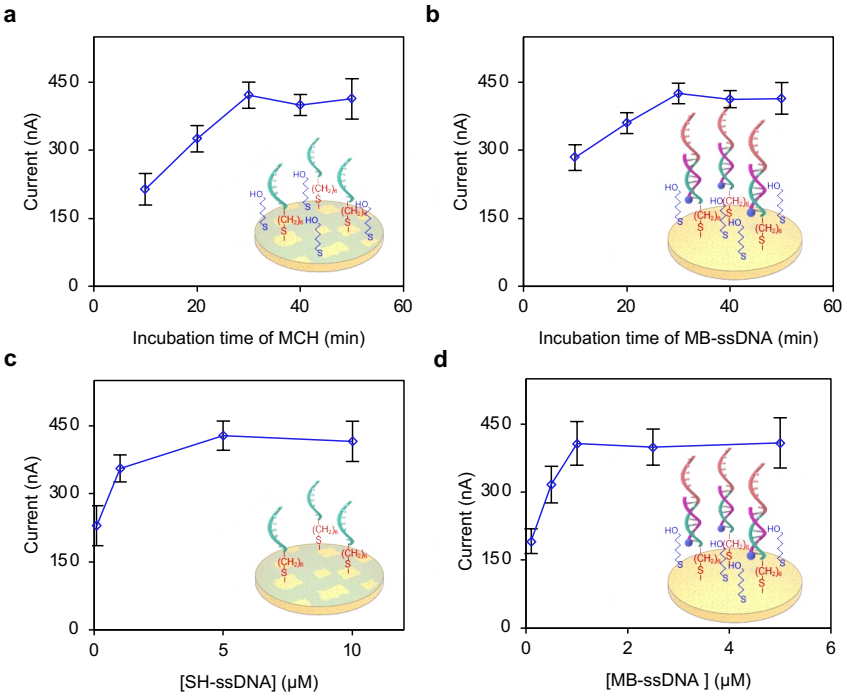

Supplementary Fig. 16 | Optimization of the preparation process of the electrochemical estradiol sensors. a,b, The influence of incubation time of MCH (**a**) and MB-ssDNA (**b**) on the peak current height of the SWV voltammograms of the estradiol sensors in 50 pM estradiol. **c,d**, The influence of reagent concentration of SH-ssDNA (**c**) and MB-ssDNA (**d**) on the peak current height of the SWV voltammograms of the estradiol sensors in 50 pM estradiol. Error bars represent the s.d. of the mean from three sensors.

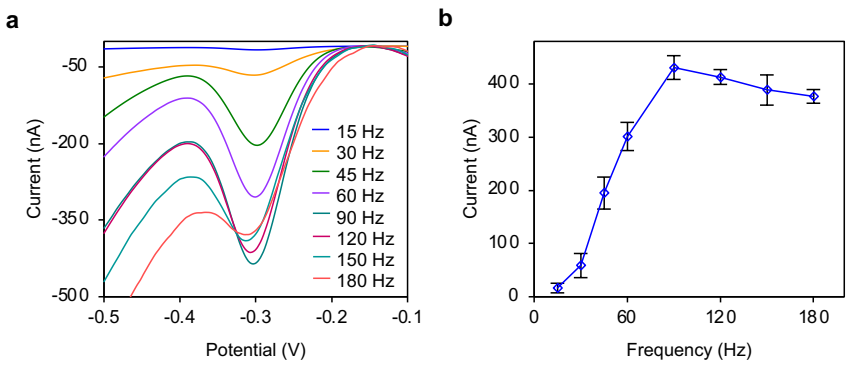

Supplementary Fig. 17 | Optimization of the measurement frequency for estradiol sensors. **a,b,** SWV voltammograms (**a**) and the corresponding peak current height (**b**) of the estradiol sensor in 50 pM estradiol under varying scan frequencies. Error bars represent the s.d. of the mean from three sensors.

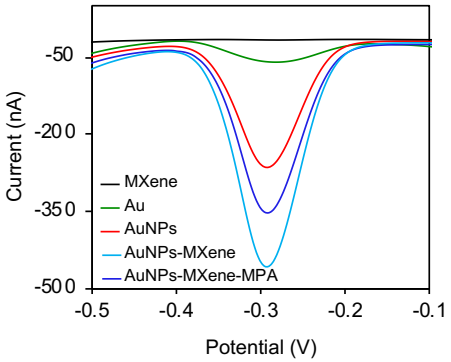

Supplementary Fig. 18 | SWV voltammograms of the estradiol sensors based on different working electrode substrates. The detection was performed in artificial sweat (0.2x PBS, pH 7.4) with 50 pM estradiol. MPA, mercaptopropionic acid.

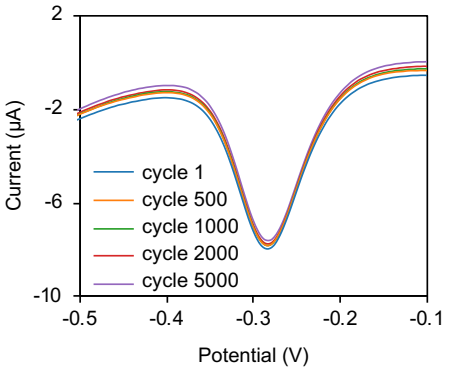

Supplementary Fig. 19 | Stability of an MB-ssDNA/SH-ssDNA modified AuNPs-MXene electrode after 5000 cycles of SWV measurement in 0.2x PBS (pH 7.4).

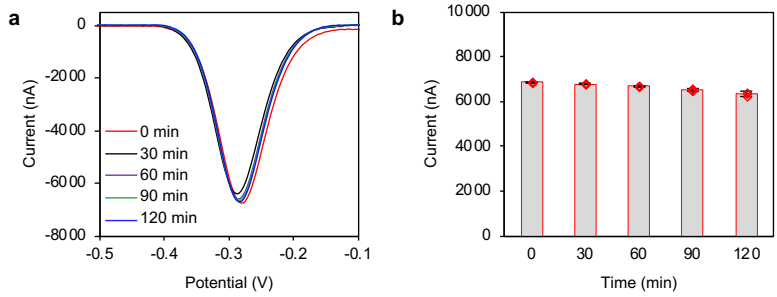

Supplementary Fig. 20 | Stability of the MB-ssDNA/SH-ssDNA modified AuNPs-MXene electrodes in solutions. a,**b**, The SWV voltammograms (**a**) and the corresponding peak current height (**b**) of the MB-ssDNA modified AuNPs-MXene electrodes after 0, 30, 60, 90, and 120 minutes of conditioning in 0.2x PBS (pH 7.4). Error bars represent the s.d. of the mean from three sensors.

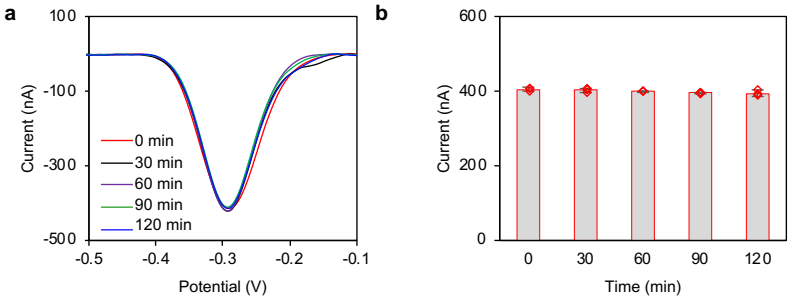

Supplementary Fig. 21 | Stability of the aptamer estradiol sensor in solutions. a,**b**, The SWV voltammograms (**a**) and the corresponding peak current height (**b**) of the aptamer estradiol sensors after target recognition (50 µM estradiol) followed by 0, 30, 60, 90, and 120 minutes of conditioning in 0.2x PBS (pH 7.4). Error bars represent the s.d. of the mean from three sensors.

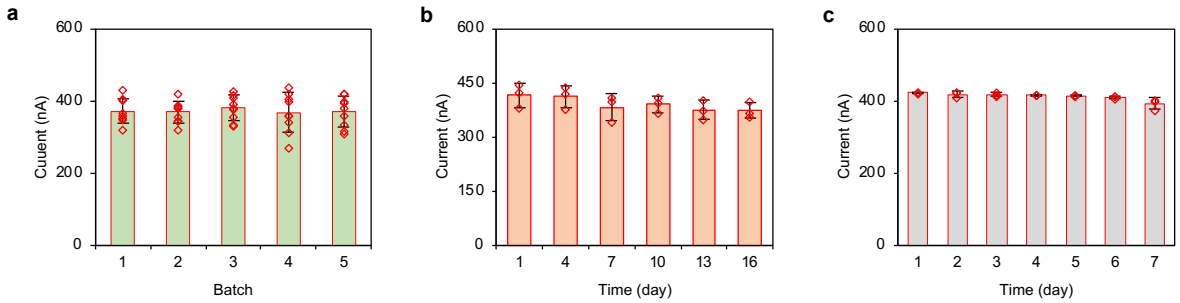

Supplementary Fig. 22 | The repeatability and storage stability of the aptamer estradiol sensor. a, The peak current height of the SWV voltammograms of the estradiol sensors from five different batches tested in artificial sweat (0.2x PBS, pH 7.4) with 50 pM estradiol. **b,** Storage stability of the estradiol sensors for detecting 50 pM estradiol over a 15-day storage period under cold condition (4 ºC). **c**, Storage stability of the estradiol sensors for detecting 50 pM estradiol over a 15-day storage period room temperature. Error bars represent the s.d. of the mean from three sensors.

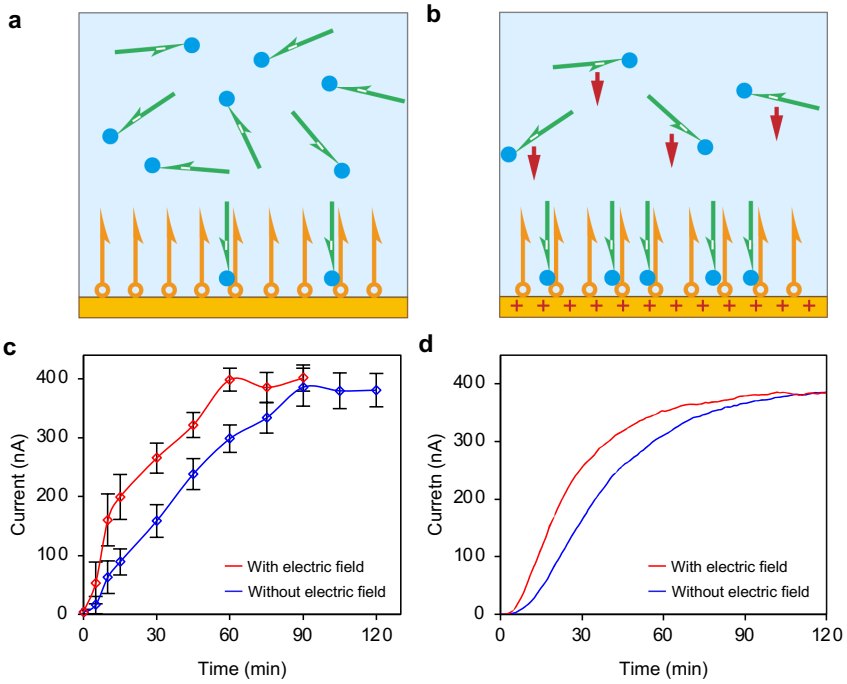

Supplementary Fig. 23 | Electric field enhanced rapid estradiol analysis. a,**b**, Schematic illustration of the enhanced MB-ssDNA transport process toward the working electrode without (**a**) and with (**b**) an external electric field. **c**,**d**, The peak current height of the SWV voltammograms of the estradiol sensors (**c**) and numerically simulated sensor performance (**d**) under varying incubation time with and without the assistance of an external electric field. Error bars represent the s.d. of the mean from three sensors.

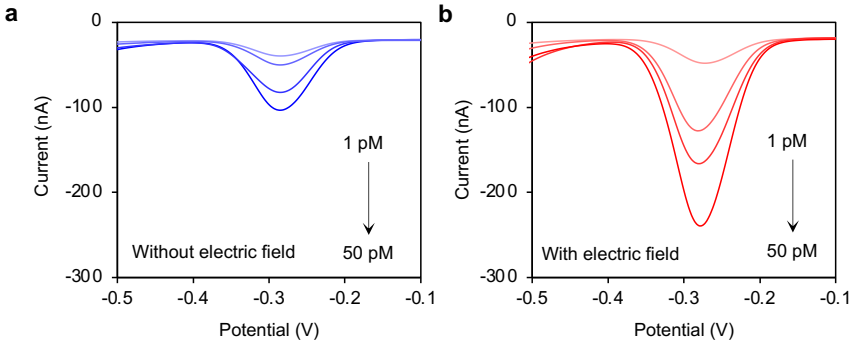

Supplementary Fig. 24 | Rapid estradiol analysis with the assistance of an external electric field. a,b, SWV voltammograms obtained with 10-minute incubation of the estradiol sensors in 1, 5, 10, 50 pM estradiol without (**a**) and with (**b**) the assistance of an external electric field.

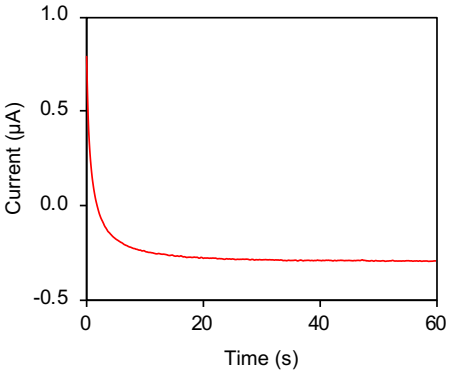

Supplementary Fig. 25 | Current-time response under a bias voltage of 0.5 V for rapid estradiol analysis.

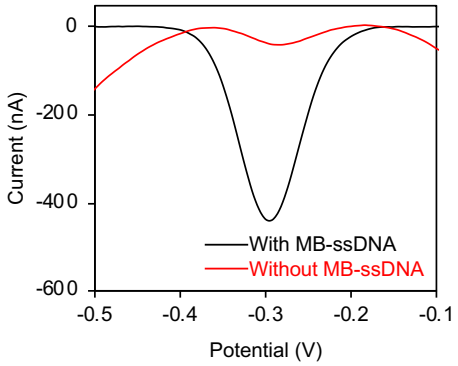

Supplementary Fig. 26 | The influence of the electrostatic adsorption of MB-ssDNA onto the positively charged detection WE upon the sensing result. The SWV voltammograms obtained from an estradiol sensor with and without SH-ssDNA modified on the detection WE. Electrochemical measurements were performed after a 60-minute incubation in 50 pM estradiol with the application of a bias-potential (1 min duration at +0.5 V prior to incubation).

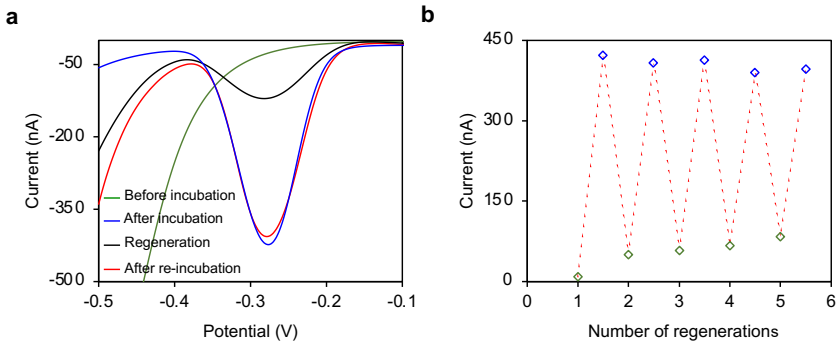

Supplementary Fig. 27 | Sensor regeneration in artificial sweat. a,b, SWV voltammograms (**a**) of the estradiol sensors for detection of 50 pM estradiol in artificial sweat (0.2x PBS, pH 7.4) and regeneration through 1-minute rinse using artificial sweat (0.2x PBS, pH 5), and the corresponding peak current height (**b**) showing the regeneration and repetitive use of the estradiol sensors.

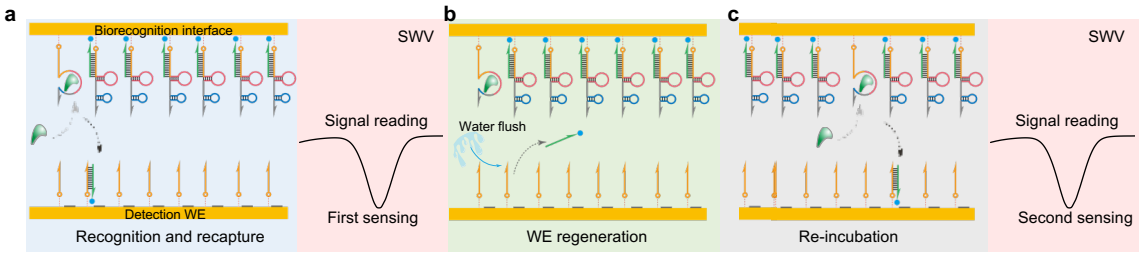

Supplementary Fig. 28 | Schematic about the in vitro sensor regeneration process.

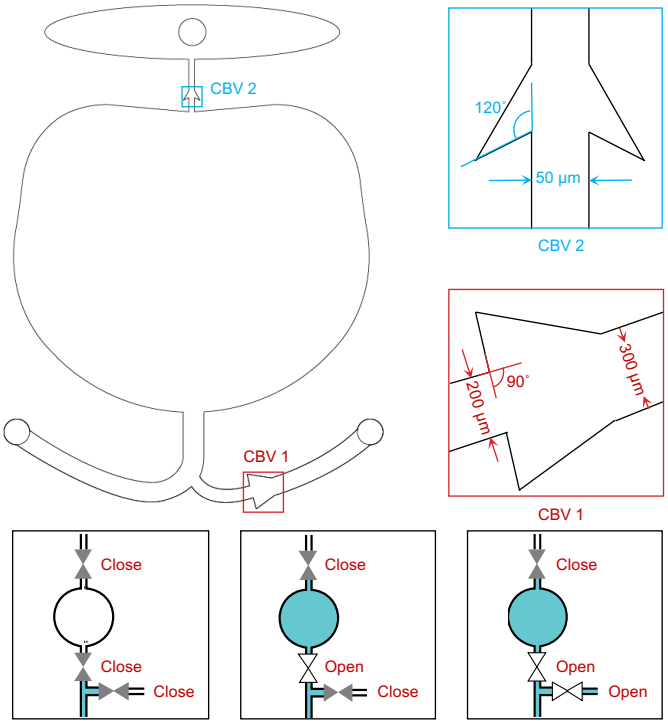

Supplementary Fig. 29 | The design and working principle of the CBVs in the wearable patch. The CBVs stay closed and block sweat at pressures lower than their bursting pressures (BPs). When sweat in the microfluidics reaches two separate CBVs with different BPs, it will first flow through the valve with lower BP. In our geometrical design, CBV1 has lower BP then CBV2. Sweat firstly flow into the microfluidics via the inlet and enters the main sensing reservoir; sweat arrives at CBV1 and CBV2 in their closed states. Once sweat fully fills the reservoir, the pressure at CBV1 and CBV2 increases and reaches the bursting pressure of CBV1 first. In this case CBV1 opens to allow new sweat to flow through and eventually flow out through the outlet. During the entire sensing period, CBV2 remains closed (the purpose of CBV2 is to balance air pressure and allow sweat to enter and fill the sensing reservoir first). Such microfluidic valving design allows highly stable biosensing in the quiescent sweat matrix in the sensing reservoir free from the influence of sweat flow.

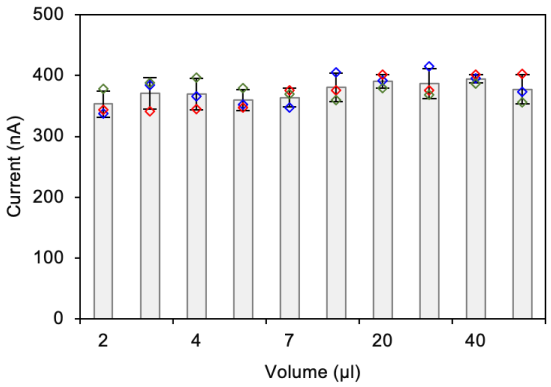

Supplementary Fig. 30 | The influence of sample volume on sensor performance. Figure illustrates the current of the SWV peak current height of the sensors measured in 50 pM estradiol with varying sample volumes (2, 3, 4, 5, 7, 10, 20, 30, 40, 50 µl). Data are shown as mean ± s.d. (n = 3).

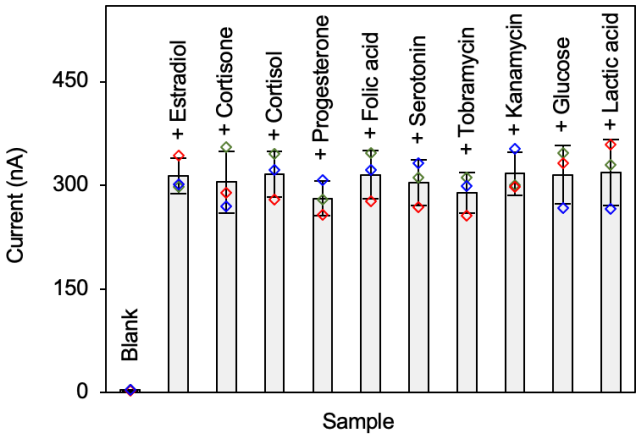

Supplementary Fig. 31 | Selectivity of the microfluidic sensors to potential interferences in human sweat. 50 pM estradiol and interferent molecules were used. Data are shown as mean ± s.d. (n = 3).

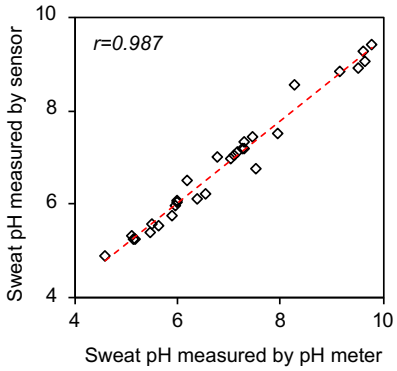

Supplementary Fig. 32 | Validation of the pH sensor with a commercially available pH meter for sweat sample analysis. n=31 biologically independent samples.

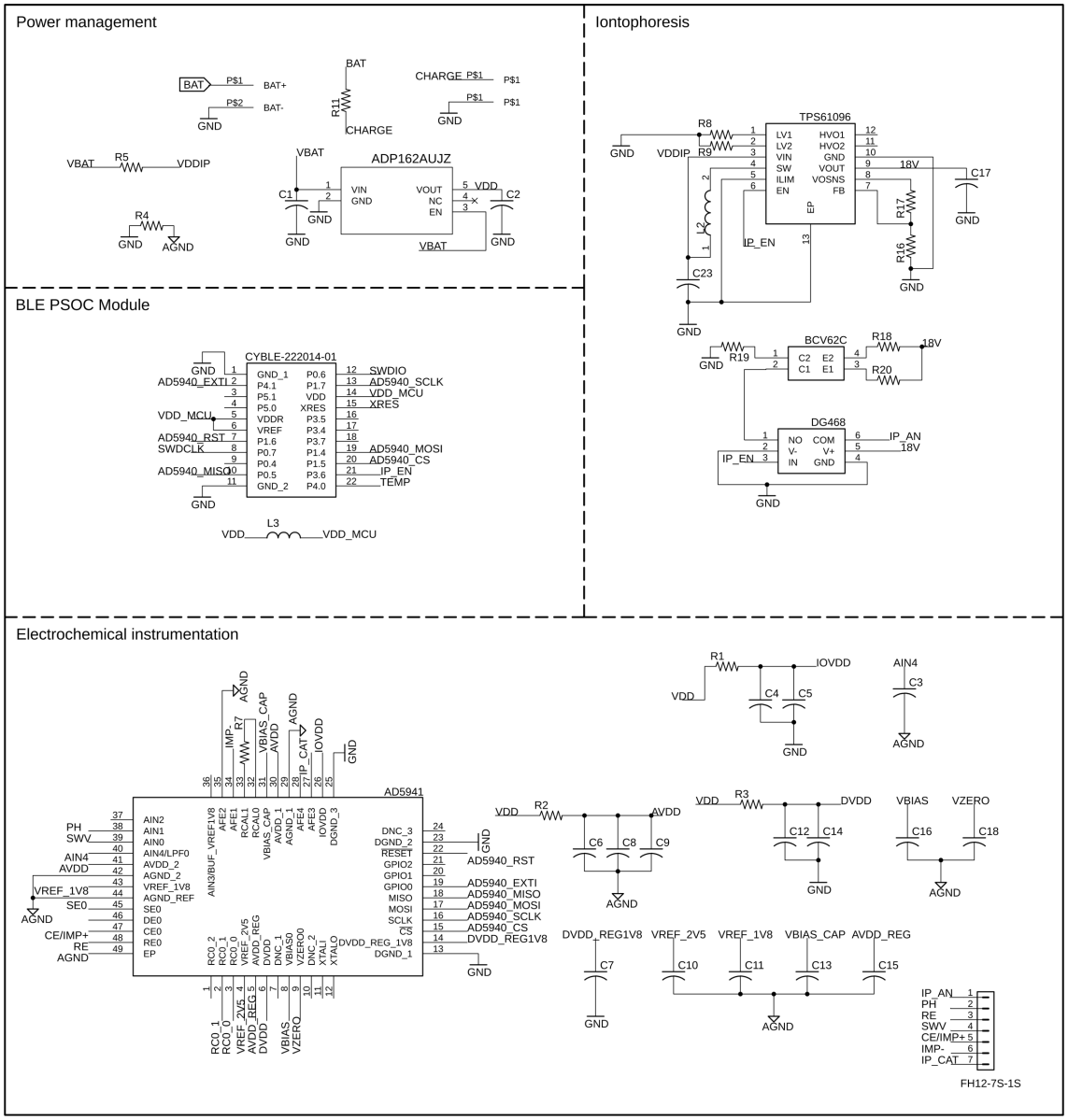

Supplementary Fig. 33 | Detailed circuit diagram of the integrated electronic system for wearable estradiol sensing.

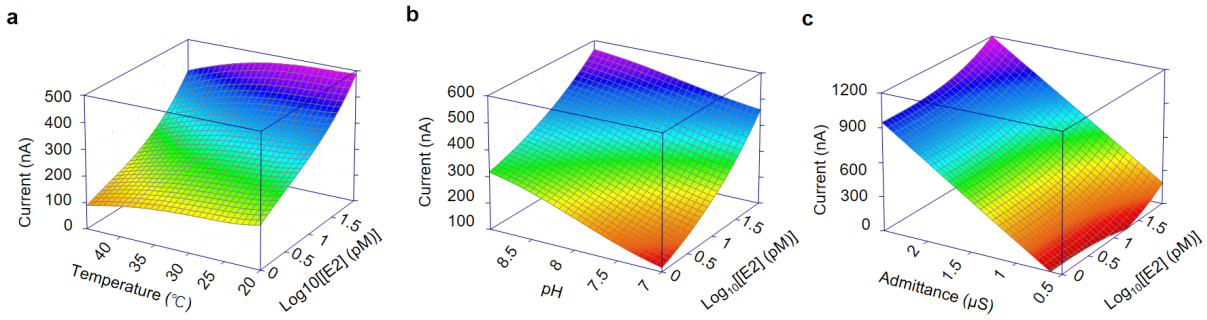

Supplementary Fig. 34 | The performance of the aptamer sensors under different temperature, pH and ionic strength levels. a–c, Color maps showing the dependence of aptamer sensor response (SWV peak current height) on temperature (**a**), pH (**b**), and ionic strength (**c**).

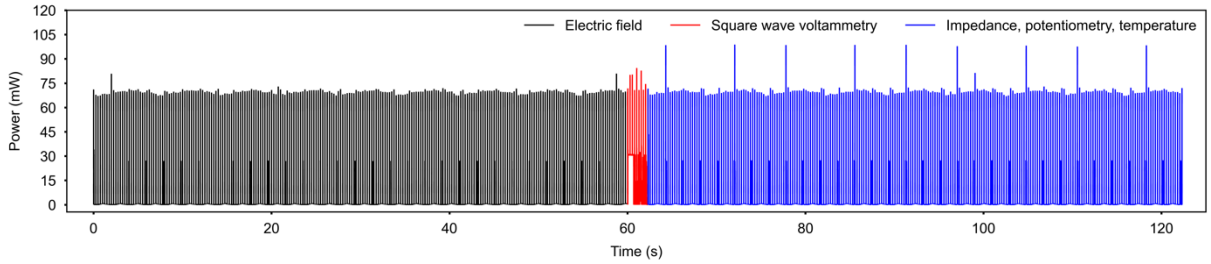

Supplementary Fig. 35 | The operation power consumption profiles of the modules of wearable estradiol sensor.

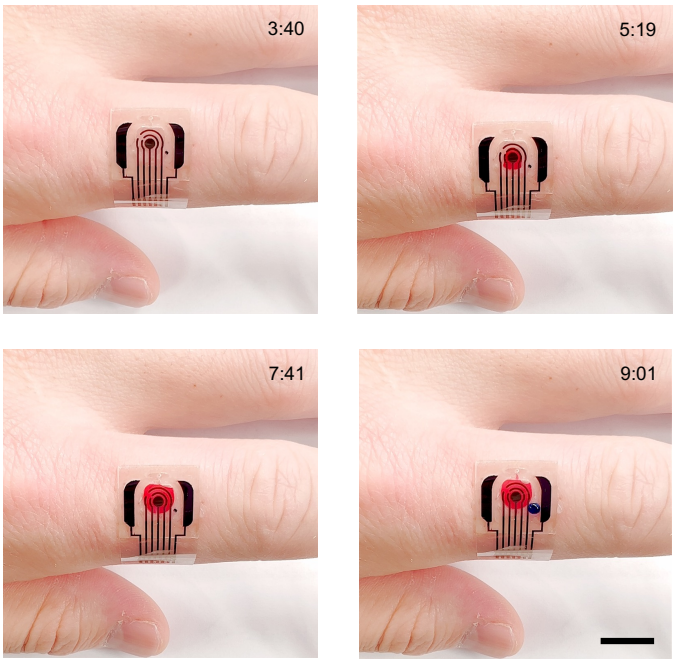

Supplementary Fig. 36 | Time-lapse images of the microfluidic sampling of the iontophoresis-induced sweat using a finger-worn wearable sensor for automatic hormone analysis. Scale bar, 1 cm.

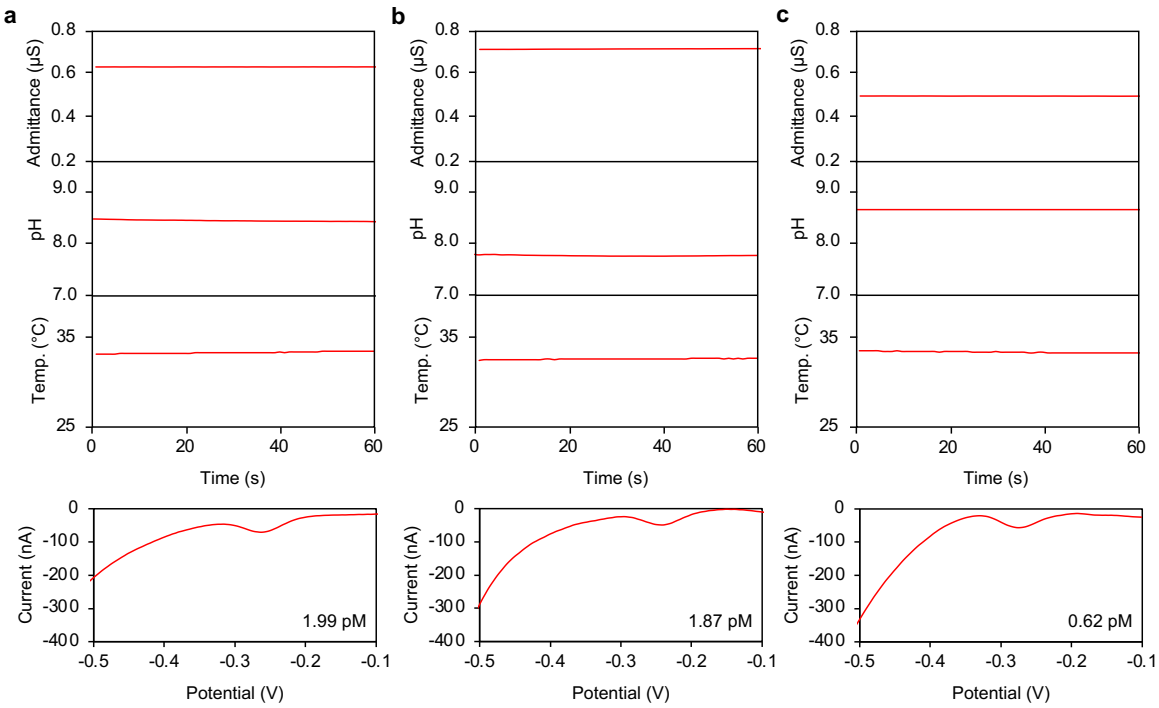

Supplementary Fig. 37 | On-body wearable multiplexed physicochemical sensing and estradiol quantification in three male human subjects. Male subjects were used here as the control (compared to the female subjects in **Fig. 4**).

Supplementary Table 1 | The ink formulation of the employed AuNP ink.

Chemical name	% by Weight
Gold	9-11
Deionized water	36-40
Glycerol	48-52
Alcohol	0.1-1.0
Polyoxyalkylene alkyl ether	0.05-0.5
Nonionic surfactant	0.05-0.5

Supplementary Table 2 | The ink formulation of the employed MXene ink.

Chemical name	% by Weight
Ethylene glycol	49.5
Deionized water	49.5
MXene	1

Supplementary Video 1 | Numerical simulation of the electric field enhanced estradiol sensing.

Supplementary Video 2 | Microfluidic sweat sampling using a finger-worn wearable sensor patch.

Supplementary Video 3 | Real-time wireless estradiol monitoring.